Journal of Biomedical Optics 7(1), 72–79 (January 2002)

Multispectral near-infrared tomography: a case study in compensating for water and lipid content in hemoglobin imaging of the breast

Troy O. McBride
Brian W. Pogue
Dartmouth College
Thayer School of Engineering
Hanover, New Hampshire 03755

Steven Poplack
Sandra Soho
Dartmouth-Hitchcock Medical Center
Department of Radiology
Lebanon, New Hampshire 03766

Wendy A. Wells
Dartmouth-Hitchcock Medical Center
Department of Pathology
Lebanon, New Hampshire 03766

Shudong Jiang
Ulf L. Österberg
Keith D. Paulsen
Dartmouth College
Thayer School of Engineering
Hanover, New Hampshire 03755

Abstract. Images of hemoglobin concentration and oxygen saturation are presented from multispectral near-infrared tomographic measurements in the breast of a woman with an invasive cancer. Images of the absorption coefficient and reduced scattering coefficient are recovered from the measured data using a finite element reconstruction algorithm based on the frequency-domain diffusion equation. Three methods of recovering the hemoglobin concentration and oxygen saturation images are presented which compensate for water and lipid absorption in different ways: (1) an assumed bulk content of water and lipids is used, (2) four chromophores are imaged, and (3) scattering power data are applied to deduce water and lipid images. In all three cases, a large increase in the hemoglobin concentration (3:1) is observed at the location of the cancer while a maximum of 15% difference is observed in the hemoglobin images between each of these methods for water and lipid compensation. [DOI: 10.1117/1.1428290]

Keywords: optical tomography; diffuse imaging; breast cancer; finite element; near-infrared; hemoglobin.

Paper JBO-10201 received Feb. 15, 2001; revised manuscript received Aug. 16, 2001; accepted for publication Aug. 23, 2001.

1 Introduction

Near-infrared (NIR) *in vivo* measurements and imaging studies have shown a high absorption contrast (2:1 to 4:1) exists between some breast cancers and the surrounding normal tissue.[1–3] This contrast is assumed to originate from an increased hemoglobin concentration at the site of breast cancers due to angiogenisis.[1,4] It is currently unknown whether this contrast will be sufficient to detect and or characterize small, early stage breast carcinoma. Other NIR parameters, such as oxygen saturation and scattering contrasts, are also being investigated as a means to differentiate benign from malignant breast disease.[5,6]

Despite evidence of high contrast, NIR imaging is confounded by high scattering such that spatial resolution is currently limited. In addition, light is attenuated similarly for both absorption and scattering heterogeneities making quantitative absorption imaging challenging. The use of frequency-domain and time-resolved techniques to obtain pathlength information, in combination with model-based iterative reconstruction methods, allows for the separation of absorption and scattering heterogeneities[7] and improves spatial resolution and contrast.[8,9] Currently, the resolution limits of the NIR method are unclear, however, moderate-resolution quantitative images of absorption, scattering, and hemoglobin parameters[10] have been obtained in phantom studies suggesting that clinically useful *in vivo* quantitative hemoglobin imaging can be achieved.[2,9]

Several groups worldwide are pursuing NIR imaging of the breast with moderate success.[2,3,11–14] No group has yet to definitively show a diagnostic value from NIR tomographic imaging of the breast. Several studies have anecdotally obtained similar sensitivity and specificity to x-ray mammography, and considering the widespread placement, acceptance, and the low dose rates of modern x-ray machines, some NIR studies have been discontinued. Interest remains, however, for NIR quantitative hemoglobin imaging,[2] dynamic imaging,[11] imaging with contrast agents,[12] and incorporating structural information from high resolution imaging modalities to improve the resolution and accuracy of NIR hemoglobin images.[15] Not surprisingly, it is areas such as measuring the hemoglobin content, which provide a different type of information than the structural changes seen with conventional imaging (i.e., mammography and breast sonography), that show the most promise for future clinical application.

For static NIR imaging, without the addition of contrast agents, absorption coefficient (μ_a) images are primarily related to the spatial distribution of oxygenated and deoxygenated hemoglobin ($Hb{-}O_2$ and $Hb{-}R$) contrast,[16] and to a lesser extent water and lipid content.[17] Measurement at multiple optical wavelengths permits the imaging of these components as their absorption spectra are sufficiently different. A particular ''bench to bedside'' challenge for NIR breast chromophore imaging is transitioning from two spatially varying absorbers ($Hb{-}O_2$, $Hb{-}R$) to four (additionally, water and lipids). In some NIR tomographic imaging configurations it may prove difficult to acquire μ_a images at a sufficient num-

Address all correspondence to: Troy O. McBride. Present address: Vassar College, Department of Physics and Astronomy, Poughkeepsie, NY 12604; Tel: 845-437-7341; E-mail: mcbride@vasser.edu

1083-3668/2002/$15.00 © 2002 SPIE

ber of wavelengths to recover the concentration of these four chromophores. In a previous simulation study, we estimated that a minimum of four wavelengths is needed just to recover accurate images of Hb−R and Hb−O_2 in the presence of noise.[10] In lieu of additional wavelengths, however, it may be possible to use scattering information to estimate water and lipid content.[18] The wavelength (λ) dependence of the reduced scattering coefficient (μ_s') can be approximated as a power relationship. By performing a fit to ln(μ_s') vs ln(λ), images of scattering ''power'' can be determined, as defined by the slope of this data fit. From NIR point measurements at UC-Irvine's Beckman Laser Institute,[18] it appears that the scattering power is linearly related to the water and lipid content in the breast. Thus, scattering power images might be used to determine both the water and lipid spatial content reducing the total number of wavelengths necessary for the separation of Hb−O_2, Hb−R, water, and lipids.

In this paper, we present recent clinical images obtained from a multispectral NIR tomographic imaging system developed at Dartmouth College. The system has evolved to a point where moderate resolution quantitative images of absorption, scattering, and consequently hemoglobin concentration and oxygen saturation are obtained consistently in tissue-simulating phantoms.[19] Data have been acquired from approximately 40 women as the imaging system has been developed, including 20 with the current experimental setup. Here, we display images from one woman with a mammographically subtle 3 cm invasive left breast cancer as a means of presenting the clinical status of the setup and demonstrating the potential of quantitative hemoglobin imaging with NIR light. With the presentation of these images, we also explore some of the challenges in achieving quantitative hemoglobin images within the breast. In particular, we explore three methods of compensating for a limited number of optical wavelengths, and the broad spectral signatures in the 660−830 nm region, in determining the unknown spatial content of water and lipids and its effect on hemoglobin imaging.

2 Methods

2.1 Data Acquisition

For breast imaging, the woman lies prone on a custom-built patient bed which is a modified massage table with padding. The breast to be imaged is placed pendant through a 20 cm diameter hole. A series of machined plastic inserts with a range of central openings (20, 18, 15, 13, and 10 cm) are used to comfortably support the pendant breast that varies in size, while maximizing the access of the fiber-optic array to the length of the breast, thereby allowing imaging as near the chest wall as possible. (The top of the 6 mm detector fiber bundle can be placed within approximately $\frac{1}{4}$ inch of the chest wall.) A photograph of the examination table is shown in Figure 1.

The frequency-domain data-acquisition system is centered under the opening in the patient platform. A 16 source, 16 detector circular array of fiber-optic bundles is positioned in direct contact with the breast tissue surface. Alternating source and detector optical fibers are arranged in a circular geometry and translated by 16 radially-arranged linear translation stages to acquire a single coronal tomographic plane through the breast. The fiber-optic patient interface is shown in Figure 2. The radially-mounted stages are attached to a vertical positioner which allows for the selection of a tomographic plane from the chest wall to the nipple. Four push buttons control the vertical (up/down) and radial position (in/out) of the fiber-optic array to allow positioning by the exam attendant. The translation stage system was custom-built (Velmex, Inc., Bloomfield, NY) to position the fibers with a high degree of accuracy and precision.

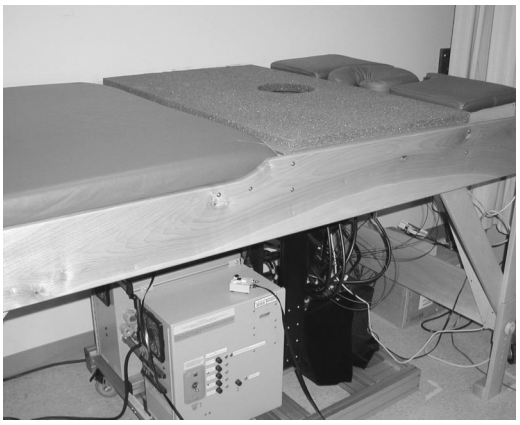

Fig. 1 Photograph of the custom-built patient bed which is a modified massage table with padding. The patient lies prone on the examination table with her face cradled in the headrest shown at the top of the figure. The breast to be imaged is placed pendant through the 20 cm diameter circular opening. The fiber-optic patient interface and detection array are aligned directly below the opening in the examination table.

Four laser diodes (761, 785, 808, and 826 nm) are used to deliver 100 MHz amplitude-modulated light through a fiber combiner to a rotary stage where the light is multiplexed serially to each of the source fibers. The direct current and radio frequency (rf) power to each laser is applied serially through a computer-controlled rf switch. Sixteen photomultiplier tubes (PMTs) are mounted to the same rotary stage for detection. The large change in light level between near and far detectors is compensated by the computer-controlled gain of the PMTs. The PMTs are rotated with respect to the detector fiber bundles such that their position relative to the source is fixed, thus the gains of the PMTs are set only once per acquisition session. Each PMT signal is input into a separate rf mixer

Fig. 2 The fiber-optic patient interface is shown. The larger black cables are the detector fiber-optic bundles. The fiber optics are mounted on posts connected to a series of translation stages mounted radially.

mounted on the rotary stage and mixed with a 100.0005 MHz reference signal. The resulting 500 Hz signal is amplified and low-pass filtered prior to lock-in detection within the computer. For a single tomographic plane, 256 measurements of phase and amplitude are recorded and processed by a finite element (FEM) program to reconstruct images of μ_a and μ_s'. The full description of the construction of this data-acquisition system can be found in a previous publication.[20]

2.2 Reconstruction Algorithm

A FEM reconstruction program based on the frequency-domain diffusion equation allows recovery of images of μ_a and μ_s' from the measured data. The FEM solution of the diffusion equation on a circular mesh determines a calculated data set from an initial estimate of the average optical properties (μ_a, μ_s'). A Newton–Raphson minimization of the difference between the measured and calculated data is then applied to recover the true distribution of optical properties. A Levenberg–Marquardt regularization scheme is used to invert the ill-posed sensitivity matrix which arises from the minimization. The initial estimate of the optical properties is obtained from a separate minimization using the same forward FEM solver but with data averaged over all source positions and the assumption of homogeneous μ_a and μ_s' throughout the circular mesh. The details of the reconstruction program and homogeneous fitting algorithm can be found elsewhere.[8,21,22]

2.3 Phantom Studies

Phantom experiments have confirmed that quantitative NIR imaging of μ_a and μ_s' is experimentally possible.[9] Further studies with human blood mixed in a highly scattering medium demonstrated that quantitative hemoglobin imaging is achievable.[19] The resolution to contrast limits of the current experimental setup was studied in a recent paper, which concluded that for an object of known size, quantitative absorption imaging can recover a 4 mm object in a 84 mm phantom with 2:1 contrast.[23] A recent study with excised breast tissue confirmed that quantitative absorption and scattering imaging is also possible in heterogeneous tissue.[24] These phantom studies lend confidence to the belief that quantitative *in vivo* imaging can be achieved in cases where the lesion diameter is more than 1/20 of the diameter of the breast, using current system parameters.

2.4 Chromophore Separation

It is widely assumed that the primary NIR absorbers in breast tissue are Hb–O_2, Hb–R, water, and lipids. The absorption spectra of these constituents, as measured by other groups,[16,17,25] are displayed in Figure 3. In general, an important goal of NIR breast imaging is assessing total hemoglobin concentration ([Hb–T] = [Hb–O_2] + [Hb–R]) and oxygen saturation (StO_2=[Hb–O_2]/[Hb–T]). A particular challenge of transitioning from laboratory experiments to patient imaging is going from two spatially varying absorbers (Hb–O_2, Hb–R) to four (additionally, water and lipids). In past studies, we have assumed a bulk water and lipid content based on average values for breast tissue. While this assumption reduces the overall error in comparison with ignoring water and lipid absorption, it is clear that the lipid and water content vary between individuals of the same age and in some individuals change with the aging process,[18] during the menstrual cycle,[26] and are likely spatially heterogeneous. Ideally, images of water and lipid should be recovered from the measured NIR data as well as [Hb–O_2] and [Hb–R].

In recovering images of concentration, it is assumed that μ_a at each wavelength is a linear combination of the concentration multiplied by the molar extinction coefficient of each constituent. A least-squares fit to the data using singular-value decomposition (SVD) is used to determine the recovered concentrations. It is not expected that four wavelengths are sufficient to accurately estimate the concentration of these four chromophores. In a previous simulation study, it was determined that four wavelengths were needed to recover [Hb–T] and StO_2 in the presence of noise.[10] Indeed, the spectra of water, lipids, Hb–R, and Hb–O_2 are broad and somewhat similar in the region of 650–830 nm. In lieu of additional wavelengths, however, it is possible that scattering information may be used to estimate the water and lipid content. Preliminary results from Cerussi et al.[18] indicate that the lipid and water content may be determined from spatially-averaged spectral scattering data.

From Mie theory calculations for a distribution of spherical scatterers, van Staveren et al.[27] empirically showed a linear relation to $\ln(\mu_s')$ vs $\ln(\lambda)$. Cerussi et al.[18] at UC-Irvine have used this same relationship with NIR point measurements of μ_s' in the breast. Equation (1) relates scattering coefficient wavelength dependence $[\mu_s'(\lambda)]$ by a constant "scattering amplitude" (A) and a "scattering power" (SP):

$$\mu_s'(\lambda) = A\lambda^{-\mathrm{SP}}. \tag{1}$$

Using data from 28 women, Cerussi et al. show a linear relationship for both the lipid and water content to SP with a coefficient of determination (r^2) of 0.84 and 0.85. The equations of the linear relations are

$$\text{Water } \% = 0.35*\mathrm{SP} - 0.05, \tag{2a}$$

$$\text{Lipid } \% = -0.50*\mathrm{SP} + 0.90. \tag{2b}$$

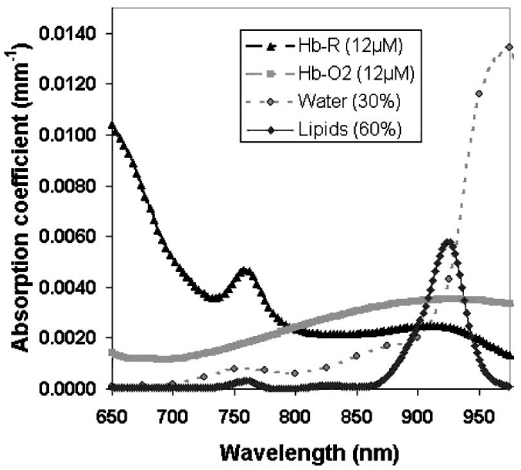

Fig. 3 Absorption spectra of Hb–R, Hb–O_2 (see Ref. 16), water (see Ref. 25) and lipids (see Ref. 17). The curves are shown for concentrations typical in breast tissue.

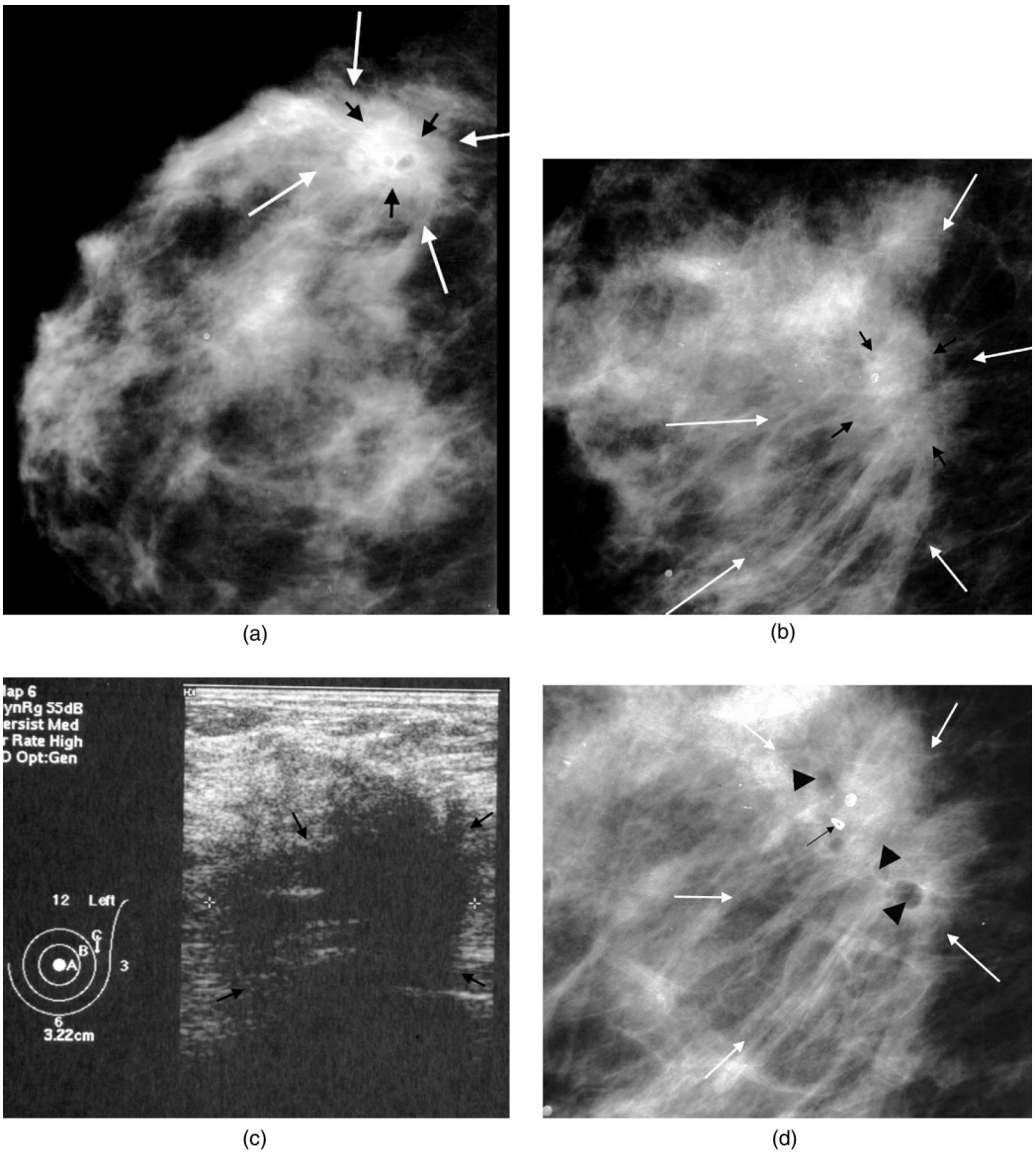

Fig. 4 (a) Digital photography of standard left craniocaudal mammogram, (b) magnified close-up mediolateral mammogram, (c) ultrasound of the tumor in the sagital plane, and (d) magnified left mediolateral mammogram following biopsy and site marker placement. White arrows delineate the area of architectural distortion reflecting tumor, while short black arrows show the central tumor mass. In (d), the thin black arrow denotes the biopsy site marker clip and the large black arrowheads show air at the biopsy site.

Table 1 Values for StO_2 and [Hb–T] for different methods of compensating for water and lipid content. Method 1, the assumption of a fixed bulk water and lipid content, corresponds to Figure 5. Method 2 (Figure 6) involves a least-squares fit to all four chromophores. Method 3 (Figure 7) uses the scattering power image to image water and lipids. Method 4 assumes no lipid and water content.

	Average Values				Value at center of lesion	
Method	[Hb-T] (μM)	StO_2 (%)	Water (%)	Lipid (%)	[Hb-T] (μM)	StO_2 (%)
1	19	65	30	60	56	65
2	22	70	4	136	53	74
3	19	63	30	39	58	65
4	22	63	0	0	60	64

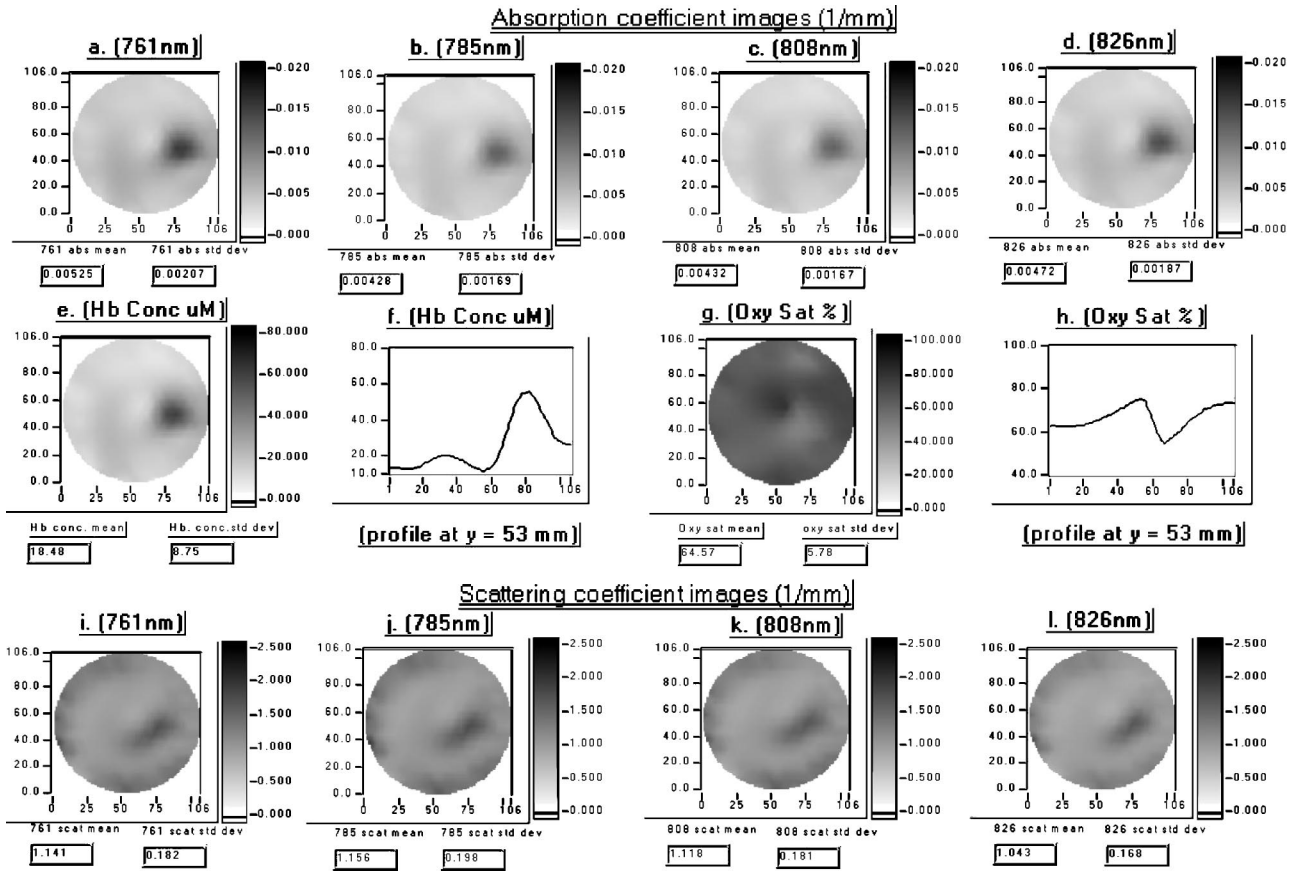

Fig. 5 Tomographic NIR images of female breast with 3 cm lesion located at 3 o'clock presented in the manner used by our clinical database. (a)–(d) and (i)–(l) are μ_a and μ_s' images (in grayscale units of 1/mm) at the four wavelengths indicated. (e) and (g) are [Hb–T] and StO_2 images determined using method 1 (assumption of 30% and 60% bulk water and lipid content). The *x* and *y* axes of the images are position in units of millimeters. The average values and standard deviation of all pixels are indicated below each image. (f) and (h) are horizontal transects through the center of images (e) and (g).

This relationship can be used to approximate bulk water and lipid content or may be applied to each point in the image to determine the water and lipid content spatially.

We present results from three methods of determining [Hb–T] and StO_2 images based on different treatments of the water and lipid content. These are: (1) the water and lipid content are assumed to be constant at 30% and 60% respectively;[19] (2) a fit is performed to all parameters, Hb–R, $Hb–O_2$, water, and lipids based on absorption data at four wavelengths; and (3) scattering power is used to image water and lipids before fitting for Hb–R and $Hb–O_2$ from absorption data at four wavelengths. These results are compared with the assumption of no lipid and water absorption (method 4 in Table 1) to assess the potential variation involved in the method of estimating the water and lipid content.

2.5 Patient Imaging

Conventional and NIR imaging results are presented for a single 73 year old female volunteer. The subject underwent routine mammography, which demonstrated a 2.5 cm (maximal diameter) focal ill-defined density with a larger (approximately 6 cm maximal diameter) area of associated architectural distortion situated in the deep lateral left breast [Figures 4(a) and 4(b)]. Breast ultrasonography directed to the lateral left breast confirmed an irregular hypoechoic mass with acoustic shadowing [Figure 4(c)]. The imaging abnormality corresponded to a palpable lump in the lateral left breast. An ultrasound guided 11 gauge vacuum assisted needle biopsy of the mass was performed 2 weeks prior to NIR imaging, establishing the diagnosis of an invasive ductal carcinoma. A 2 mm (maximal diameter) × 0.2 mm (approximate thickness) stainless steel marker clip, (Micromark 2 tm [Ethicon]), was placed in the mass at the time of the needle biopsy, and demonstrated mammographically immediately following the biopsy [Figure 4(d)]. Subsequent (1 week after NIR imaging) therapeutic lumpectomy and left axillary sentinel lymphadenectomy revealed a 5.9 cm low grade invasive ductal carcinoma without (0/2) axillary nodal metastases.

For the NIR exam, the research nurse aligned the NIR imaging array in the coronal plane of the palpable lump of the pendant left breast. The fiber-optic array was brought in direct contact with the breast using push-button controls. Three planes of tomographic data were acquired: at the midline of the lesion, 1.3 cm above, and 0.9 cm below the midline. Data were also acquired from the contralateral normal right breast at a single coronal imaging plane corresponding to the location of the left breast lesion based on the depth from the chest wall to the imaging array.

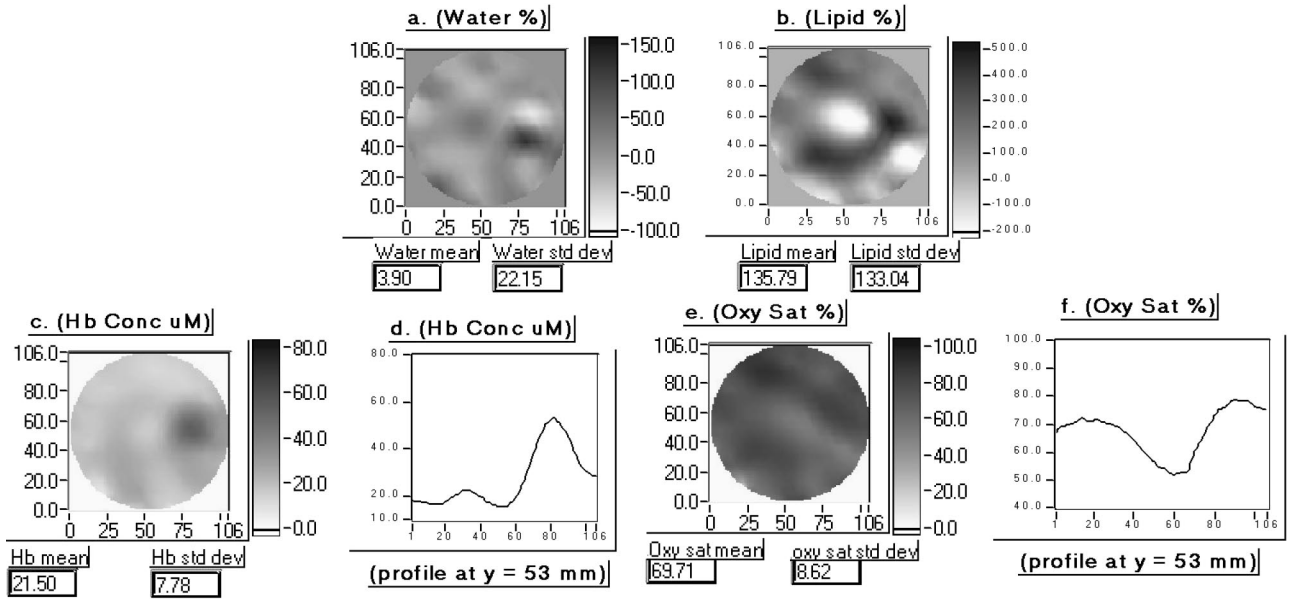

Fig. 6 Images of (a) water, (b) lipids, (c) [Hb–T], and (e) StO_2 are recovered using a least squares fit to determine all four parameters (method 2) from the μ_a images presented in Figure 5. The *x* and *y* axes of the images are position in units of millimeters. (d) and (f) are horizontal transects through the center of images (c) and (e).

3 Results

The results for the female volunteer images (acquired at the midline of the lesion) are presented in Figure 5 in the typical format submitted to our clinical database. Here, μ_a and μ_s' images at the four wavelengths are displayed. Initially a constant water and lipid concentration of 30% and 60%, respectively, was assumed and the relevant values subtracted from the μ_a images prior to determining distributions of [Hb–T] and StO_2 from the SVD least squares fit for Hb–R and Hb–O_2. The lesion is clearly visible in both the μ_a and [Hb–T] images, as well as at a lower contrast in the μ_s' images. A horizontal profile through the lesion shows a peak hemoglobin concentration of 56 micromolar (μM) compared with an average [Hb–T] of 19 μM.

A second fit was performed to the μ_a images with all four quantities, [Hb–O_2], [Hb–R], lipids, and water, as free parameters. The results are presented in Figure 6. Values of lipid content range as low as −200% and as high as 500%, while water content values also range well below 0%. Though the fit failed to produce meaningful results for lipids and water, the hemoglobin images fall within a reasonable range of values.

In the third method, scattering power images were determined by performing a linear regression to $\ln(\mu_s')$ and $\ln(\lambda)$ for each image point. The resulting map of SP is displayed in Figure 7. In addition, images of lipid and water were determined from the relationships in Eqs. (2a) and (2b). Similar to the first method, the corresponding water and lipid values are subtracted and [Hb–T] and StO_2 determined from the μ_a images. The images for [Hb–T] and StO_2 are also presented in Figure 7. Table 1 summarizes the results for the three methods, while also presenting data from a fit that ignores the water and lipid content all together. In the table, the average values for the water, lipid, [Hb–T], and StO_2 images are presented as well as the value for [Hb–T] and StO_2 at the center of the lesion ($x = 82$ mm, $y = 53$ mm) based on the NIR image.

In Figure 8, the images of the contralateral normal breast are presented. Only the 761 and 808 nm μ_a and μ_s' are shown as they are representative of the other wavelengths. Also displayed are the [Hb–T] and StO_2 images using method 1 with a fixed water and lipid content of 30% and 60%.

4 Discussion

Images of [Hb–T] and StO_2 are presented from multispectral near-infrared tomographic measurements of the breast. Three methods of compensating for the lipid and water absorption with a limited number of wavelengths are described. Each method results in a similar hemoglobin concentration image with a contrast of approximately 3:1 at the location of the malignant tumor. Values for both the oxygen saturation and hemoglobin concentration change by less than 5% between method 1 (assumed bulk water and lipid content) and 3 (images of water and lipid obtained from scattering power), but by as much as 15% for the other two approaches (fit to all four chromophores and assumption of no water and lipid content). The images of the contralateral normal breast exhibit no striking contrast features.

The hemoglobin values for the invasive ductal carcinoma may be affected by the presence of the stainless steel site marker and/or the host inflammatory response to the needle biopsy procedure occurring 2 weeks prior. The metal clip was studied in phantom experiments and found to have a minimal effect when imaged inside a 84 mm tissue-simulating object. The contribution of the host inflammatory response to the NIR findings is unclear. Future studies will be performed prebiopsy and postbiopsy to assess the influence of these potential confounding circumstances upon the resulting hemoglobin images. A systematic clinical trial, which is scheduled to be-

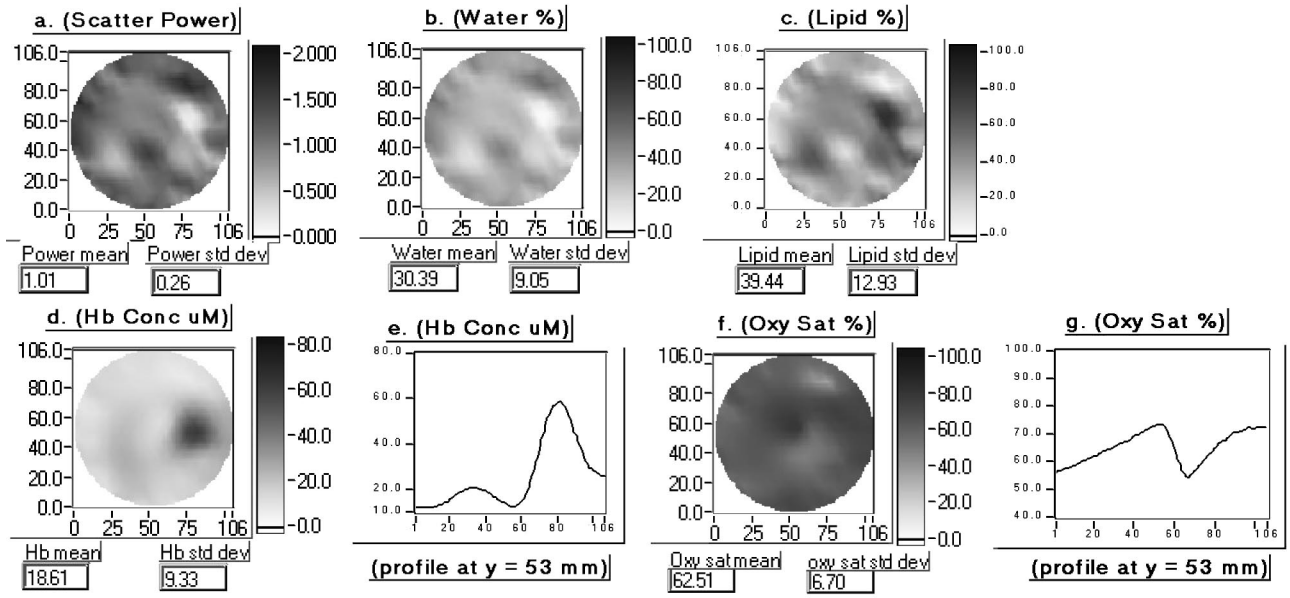

Fig. 7 Images of (a) scattering power (b) water, (c) lipids, (d) [Hb–T], and (f) StO_2 are recovered using method 3. The scattering power image is calculated from a fit to $\ln(\mu_s')$ for the sequence of images in Figure 5 vs $\ln(\lambda)$. The water and lipid images are then determined from Eqs. (2a) and (2b). The *x* and *y* axes of the images are position in units of millimeters. (e) and (g) are horizontal transects through the center of images (d) and (f).

gin in 2002, will be performed prior to biopsy.

While a larger number of optical wavelengths may be the key to good separation of breast chromophores, NIR diode lasers at additional optical wavelengths in the limited region of PMT sensitivity require additional acquisition time, are often difficult to locate, and add to system expense. Using scattering power information to infer water and lipid content may be sufficient for achieving accurate hemoglobin images. It is possible some hybrid of frequency-domain and continuous-wave imaging could improve spectral range, as noted by Bevilacqua et al.[28]

It is not clear that the assumption of a linear relation between lipid, water, and scattering power will hold over the entire female population or when applied to spatially resolved images. The method appears to provide a reasonable estimate of the lipid and water content. It is likely that tumor water and lipid content will be different than surrounding tissue and thus spatially resolving these constituents will be necessary for

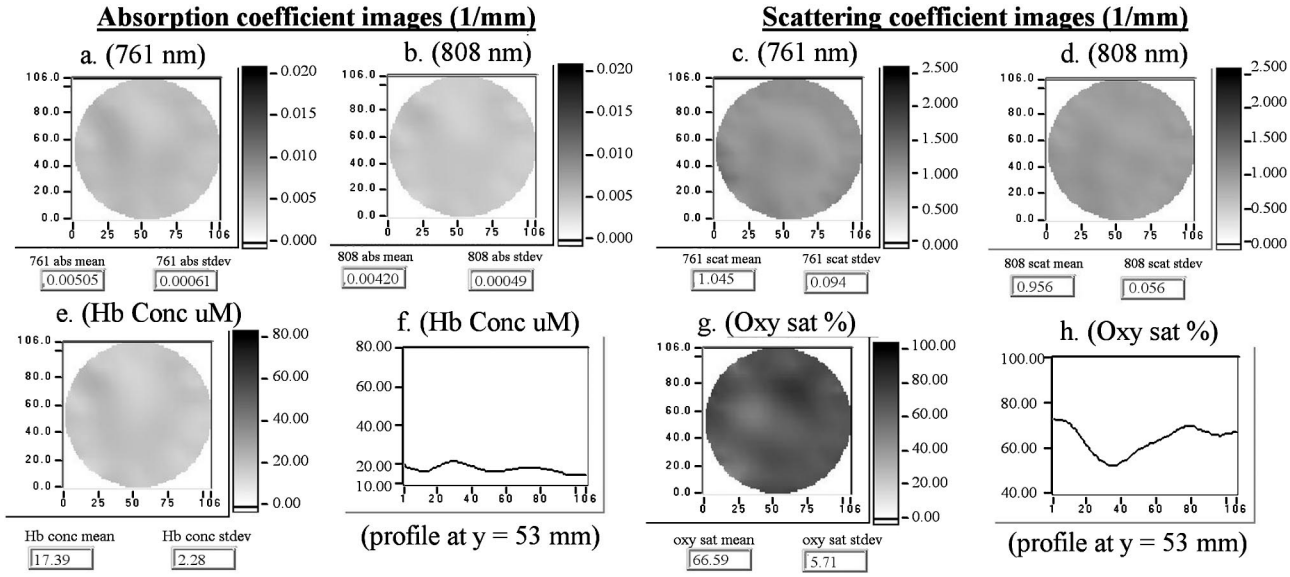

Fig. 8 Tomographic NIR images of the contralateral normal female breast. (a)–(b) and (c)–(d) are μ_a and μ_s' images (in grayscale units of 1/mm) at the two wavelengths indicated (785 and 826 nm images are omitted). (e) and (g) are [Hb–T] and StO_2 images determined using method 1 (assumption of 30% and 60% bulk water and lipid content). The *x* and *y* axes of the images are position in units of millimeters. (f) and (h) are horizontal transects through the center of images (e) and (g).

achieving highly accurate hemoglobin measurements. The error introduced from bulk approximations appears initially to have about 5% to 15% influence on the [Hb–T] and StO_2 estimates. If StO_2 is useful in diagnosis, however, these errors may prove important. Without further validation, the accuracy of these methods in assessing the lipid and water content cannot be made, however, we can use these results to demonstrate the range of variability (5%–15%) in [Hb–T] and StO_2 for different methods of compensating for water and lipid for this particular patient.

Multispectral optical tomography appears capable of *in vivo* imaging of hemoglobin parameters in the breast. Preliminary results show a high contrast in the hemoglobin images of breast lesions. Because contrast between lesions and surrounding tissue appears to exist in [Hb–T], StO_2, and scattering, it seems that lesion characterization based on quantitative assessments of these parameters may be possible.

Acknowledgments

The authors would like to express their gratitude to Albert Cerussi of the Beckman Laser Institute for providing information from their scatter power experiments. This research is funded by the National Cancer Institute through Grant Nos. PO1CA80139 and R01CA69544.

References

1. B. J. Tromberg, N. Shah, R. Lanning, A. Cerussi, J. Espinoza, T. Pham, L. Svaasand, and J. Butler, ''Non-invasive *in vivo* characterization of breast tumors using photon migration spectroscopy,'' *Neoplasia* **2**, 26–40 (2000).
2. B. W. Pogue, S. P. Poplack, T. O. McBride, W. A. Wells, K. S. Osterman, U. L. Osterberg, and K. D. Paulsen, ''Quantitative hemoglobin tomography with diffuse near-infrared spectroscopy: Pilot results in the breast,'' *Radiology* **218**, 261–266 (2001).
3. S. Fantini, S. A. Walker, M. A. Franceschini, M. Kaschke, P. M. Schlag, and K. T. Moesta, ''Assessment of the size, position, and optical properties of breast tumors *in vivo* by noninvasive optical methods,'' *Appl. Opt.* **37**, 1982–1989 (1998).
4. A. E. Profio and G. A. Navarro, ''Scientific basis of breast diaphanography,'' *Med. Phys.* **16**, 60–65 (1989).
5. B. Chance, Q. Luo, S. Nioka, D. C. Alsop, and J. A. Detre, ''Optical investigations of physiology: A study of intrinsic and extrinsic biomedical contrast,'' *Philos. Trans. R. Soc. London, Ser. B* **352**, 707–716 (1997).
6. J. B. Fishkin, O. Coquoz, E. R. Anderson, M. Brenner, and B. J. Tromberg, ''Frequency-domain photon migration measurements of normal and malignant tissue optical properties in a human subject,'' *Appl. Opt.* **36**, 10–20 (1997).
7. S. R. Arridge and M. Schweiger, ''Image reconstruction in optical tomography,'' *Philos. Trans. R. Soc. London, Ser. B* **352**, 717–726 (1997).
8. H. B. Jiang, K. D. Paulsen, U. L. Osterberg, and M. S. Patterson, ''Frequency-domain optical image reconstruction in turbid media: An experimental study of single-target detectability,'' *Appl. Opt.* **36**, 52–63 (1997).
9. T. O. McBride, S. Jiang, B. W. Pogue, U. L. Osterberg, K. D. Paulsen, and S. Poplack, ''Initial studies of *in vivo* absorbing and scattering heterogeneity in near-infrared tomographic breast imaging,'' *Opt. Lett.* **26**(11), 822–824 (2001).
10. T. O. McBride, B. W. Pogue, U. L. Osterberg, and K. D. Paulsen, ''Image reconstruction of continuously varying objects and simulated breast cancer lesions,'' in *Optical Tomography and Spectroscopy of Tissue III*, B. Chance, R. Alfano, and B. Tromberg, Eds., *Proc. SPIE* **3597**, 514–525 (1999).
11. C. H. Schmitz, H. L. Graber, H. Luo, I. Arif, J. Hira, Y. Pei, A. Bluestone, S. Zhong, R. Andronica, I. Soller, N. Ramirez, S. S. Barbour, and R. L. Barbour, ''Instrumentation and calibration protocol for imaging dynamic features in dense-scattering media by optical tomography,'' *Appl. Opt.* **39**, 6466–6486 (2000).
12. V. Ntziachristos, A. G. Yodh, M. Schnall, and B. Chance, ''Concurrent MRI and diffuse optical tomography of breast after indocyanine green enhancement,'' *Proc. Natl. Acad. Sci. U.S.A.* **97**, 2767–2772 (2000).
13. Y. Painchaud, A. Mailloux, M. Morin, V. S. , and P. Beaudry, ''Time-domain optical imaging: discrimination between absorption and scattering,'' *Appl. Opt.* **38**, 3686–3693 (1999).
14. S. B. Colak, M. B. van der Mark, G. W. t'Hooft, J. H. Hoogenraad, H. S. van der Linden, and F. A. Kuijpers, ''Clinical optical tomography and NIR spectroscopy for breast cancer detection,'' *IEEE J. Sel. Top. Quantum Electron.* **5**, 1143–1158 (1999).
15. B. W. Pogue and K. D. Paulsen, ''High resolution near infrared tomographic imaging simulations of rat cranium using apriori MRI structural information,'' *Opt. Lett.* **23**, 1716–1718 (1998).
16. S. Wray, M. Cope, D. T. Delpy, J. S. Wyatt, and E. Reynolds, ''Characterization of the near infrared absorption spectra of cytochrome aa3 and hemoglobin for the non-invasive monitoring of cerebral oxygenation,'' *Biochim. Biophys. Acta* **933**, 184–192 (1988).
17. V. Quaresima, S. J. Matcher, and M. Ferrari, ''Identification and quantification of intrinsic optical contrast for near-infrared mammography,'' *Photochem. Photobiol.* **67**, 4–14 (1998).
18. A. E. Cerussi, A. J. Berger, F. Bevilacqua, N. Shah, D. Jakubowski, J. Butler, R. F. Holcombe, and B. Tromberg, ''Sources of absorption and scattering contrast for near-infrared optical mammography,'' *Acad. Radiol.* **8**(3), 211–218 (2001).
19. T. O. McBride, B. W. Pogue, E. Gerety, S. Poplack, U. L. Osterberg, and K. D. Paulsen, ''Spectroscopic diffuse optical tomography for quantitatively assessing hemoglobin concentration and oxygenation in tissue,'' *Appl. Opt.* **38**, 5480–5490 (1999).
20. T. O. McBride, S. Jiang, B. W. Pogue, U. L. Osterberg, and K. D. Paulsen, ''Development and calibration of a parallel modulated near-infrared tomography system for hemoglobin imaging *in vivo*,'' *Rev. Sci. Instrum.* **72**, 1817–1824 (2001).
21. H. Jiang, K. D. Paulsen, U. L. Osterberg, B. W. Pogue, and M. S. Patterson, ''Optical image reconstruction using frequency-domain data: simulations and experiments,'' *J. Opt. Soc. Am. A* **13**, 253–266 (1996).
22. T. O. McBride, B. W. Pogue, U. L. Österberg, and K. D. Paulsen, ''Strategies for absolute calibration of near infrared tomographic tissue imaging,'' in *Oxygen Transport to Tissue XXI*, J. F. Dunn and H. M. Swartz, Eds. (to be published).
23. B. W. Pogue, C. Willscher, T. O. McBride, U. L. Osterberg, and K. D. Paulsen, ''Contrast-detail analysis for detection and characterization with near-infrared diffuse tomography,'' *Med. Phys.* **27**, 2693–2700 (2000).
24. T. O. McBride, B. W. Pogue, W. A. Wells, S. Jiang, U. L. Osterberg, and K. D. Paulsen, ''Preliminary study of near-infrared tomographic imaging of heterogeneous media: Simulations and images of excised breast tissue,'' in *Optical Tomography and Spectroscopy of Tissue IV*, B. Chance, R. Alfano, and B. Tromberg, Eds., *Proc. SPIE* **4250**, 204–210 (2001).
25. G. M. Hale and M. R. Querry, ''Optical constants of water in the 200-nm to 200-um wavelength region,'' *Appl. Opt.* **12**, 555–563 (1973).
26. T. E. Dzendrowskyji, E. A. Noyszewski, J. Beers, and L. Bolinger, ''Lipid composition changes in the normal breast throughout the menstrual cycle,'' *MAGMA (N.Y.)* **5**, 105–110 (1997).
27. H. J. van Staveren, C. J. M. Moes, J. van Marle, S. A. Prahl, and M. J. C. van Gemert, ''Light scattering in intralipid-10% in the wavelength range of 400–1100 nm,'' *Appl. Opt.* **30**, 4507–4514 (1991).
28. F. Bevilacqua, A. J. Berger, A. E. Cerussi, D. Jakubowski, and B. J. Tromberg, ''Broadband absorption spectroscopy in turbid media by combined frequency-domain and steady-state methods,'' *Appl. Opt.* **39**, 6498–6507 (2000).